

## PAPER

[View Article Online](#)  
[View Journal](#) | [View Issue](#)Cite this: *Energy Adv.*, 2024,  
3, 2002Received 15th April 2024,  
Accepted 3rd July 2024

DOI: 10.1039/d4ya00238e

[rsc.li/energy-advances](https://rsc.li/energy-advances)

# Universal synthesis strategy for preparation of transition metal oxide electrocatalysts doped with noble metal single atoms for oxygen evolution reaction†

Jingyao Wang,<sup>a</sup> Yiming Zhu,<sup>a</sup> Xuepeng Zhong,<sup>a</sup> Zhiwei Hu,<sup>b</sup> Wei-Hsiang Huang,<sup>c</sup>  
Chih-Wen Pao,<sup>c</sup> Hongfei Cheng,<sup>ib</sup> \*<sup>a</sup> Nicolas Alonso-Vante<sup>ib</sup> \*<sup>d</sup> and Jiwei Ma<sup>ib</sup> \*<sup>a</sup>

Electrochemical water splitting is expected to be a promising solution to the growing problem of fossil fuel depletion, but is limited by the slow anodic oxygen evolution reaction (OER). Currently, nanomaterials such as Ru/Ir-based noble metal compounds have been used as highly active electrocatalysts for OER, but the high cost and scarcity hinder their wide application. Therefore, it is crucial to develop OER electrocatalysts that combine economic efficiency with high catalytic performance. In this work, we propose a universal synthesis strategy for the preparation of various noble metals-doped 3d-transition metal oxides (NM-TMO) electrocatalysts by the salt-template method. Our characterization analyses demonstrate that the noble metals are homogeneously dispersed as single atoms in transition metal oxides. Notably, Ir-doped Co<sub>3</sub>O<sub>4</sub> catalysts, with Ir content as low as 1.35 at% (Ir-Co<sub>3</sub>O<sub>4</sub>), exhibit excellent OER performance in acidic, alkaline, and neutral media, compared to commercial IrO<sub>2</sub> as well as undoped Co<sub>3</sub>O<sub>4</sub>. This work demonstrates that the synthesis method is applicable to a wide range of noble metals and 3d-transition metal oxide matrix. This method results in reduced costs by significantly decreasing the noble metal, but improving catalytic performance.

## Introduction

Hydrogen is a promising source of clean energy because of its zero-carbon emissions and high specific energy density.<sup>1,2</sup> Currently, hydrogen is produced industrially in three ways: coal gasification, steam-methane reforming, and water electrolysis. The first two methods consume a large amount of fossil fuels, causing significant carbon dioxide emissions and contributing significantly to the greenhouse effect.<sup>3</sup> Electrochemical water decomposition has been widely recognized as a clean, sustainable, and efficient strategy for hydrogen production, which is expected to replace hydrogen production from fossil fuels in

the future.<sup>4–7</sup> In water electrolysis, the cathodic and anodic reaction is the hydrogen evolution reaction (HER) and the oxygen evolution reaction (OER), respectively.<sup>8,9</sup> In particular, OER is a remarkably intricate multi-step reaction, involving the transfer of four-electrons, and its slow kinetics and high overpotential become important factors limiting the overall efficiency of water decomposition.<sup>10–14</sup> In pursuit of effectively reducing the energy barrier and improving energy conversion efficiency, researchers are committed to developing OER electrocatalysts that are both highly active and stable.<sup>15–21</sup> Currently, noble metals like Ru, Ir, and their oxides exhibit excellent electrocatalytic OER properties over a wide pH range and have been used as commercial catalysts.<sup>22–26</sup> However, it is impractical to widely use precious metal catalysts due to their scarcity and high price. Researchers have explored alternative candidates with abundant reserves and low cost for electrocatalytic OER, such as 3d-transition metal compounds, which have high abundance and unique electronic structures.<sup>27–32</sup> Among them, 3d-transition metal oxides (TMOs), such as Co, Fe, and Ni, have been widely investigated for alkaline OER, but they have the disadvantages of high overpotential, poor activity, strong metal dissolution, and poor durability in acidic electrolytes.<sup>28,33–36</sup> The working pH of the electrocatalysts severely limits their practical applications.<sup>37</sup>

<sup>a</sup> Shanghai Key Laboratory for R&D and Application of Metallic Functional Materials, Institute of New Energy for Vehicles, School of Materials Science and Engineering, Tongji University, Shanghai 201804, China.  
E-mail: [cheng\\_hongfei@tongji.edu.cn](mailto:cheng_hongfei@tongji.edu.cn), [jiwei.ma@tongji.edu.cn](mailto:jiwei.ma@tongji.edu.cn)

<sup>b</sup> Max Planck Institute for Chemical Physics of Solids, Nöthnitzer Strasse 40, 01187 Dresden, Germany

<sup>c</sup> National Synchrotron Radiation Research Center, 101 Hsin-Ann Road, Hsinchu 30076, Taiwan

<sup>d</sup> IC2MP, UMR-CNRS 7285, University of Poitiers, 4 rue Michel Brunet, 86073 Poitiers, France. E-mail: [nicolas.alonso.vante@univ-poitiers.fr](mailto:nicolas.alonso.vante@univ-poitiers.fr)

† Electronic supplementary information (ESI) available. See DOI: <https://doi.org/10.1039/d4rp00144c>

To balance the performance and cost of OER electrocatalysts, researchers have found that combining noble and nonprecious metals by doping or surface anchoring can achieve high catalytic efficiency while reducing the amount of noble metals.<sup>38–42</sup> An effective strategy is to incorporate noble metal-based nanoparticles into 3d-transition metal oxides serving as support, which can promote electronic metal-support interactions.<sup>17,43–46</sup> Hou *et al.*<sup>17</sup> designed a multi-heterostructure, which features an Ir core wrapped in an IrO<sub>2</sub> shell anchored on a Co<sub>3</sub>O<sub>4</sub> structure. This design serves as a competent electrocatalyst for acidic OER, demonstrating superior OER activity and stability compared to unsupported IrO<sub>2</sub> and Co<sub>3</sub>O<sub>4</sub>, due to the unique electron transfer from the IrO<sub>2</sub> shell and Co<sub>3</sub>O<sub>4</sub> support to Ir.

In addition to the composition of the catalyst, the size of the electrocatalyst also has a great influence on its catalytic performance.<sup>47</sup> For example, common granular catalysts suffer from problems such as inefficient utilization of atoms.<sup>17,48–52</sup> Reduction of noble metals to ultrafine clusters or even single atoms often results in catalysts with significant activity improvement.<sup>53–55</sup> These small-sized catalysts are collectively referred to as atomically dispersed catalysts (ADCs).<sup>56</sup> Within the field of catalysts, a burgeoning area of research is the exploration of ADCs. These catalysts comprise single atoms, double atoms, and clusters, obtained by various synthetic approaches. They stand out as a new frontier, as they show increased atom utilization efficiency and catalytic selectivity, which is achieved by precisely manipulating the configuration and composition surrounding the central metal atoms.<sup>57</sup> Due to the Gibbs–Thomson effect, the central metal atoms tend to aggregate into nanoclusters/particles.<sup>58</sup> The difficulty in fabricating a uniform and stable dispersion of metal atoms prevents the development of single-atom catalysts (SACs).<sup>56,59</sup> Traditional approaches to precious metal-based SACs fabrication methods often involve intricate procedures.<sup>57</sup> Hu *et al.*<sup>60</sup> proposed a method to prepare one-dimensional coral-like Ru-doped cobalt oxide nanofibers possessing high specific surface area by electrostatic spinning and subsequent heat treatment. The overpotential of Ru-doped cobalt oxide nanofibers is 300 mV in 1.0 M KOH electrolyte at room temperature, lower than that of ruthenium oxide, with the same catalyst loading. However, the electrostatic spinning process requires a very high voltage to be carried out and strict control of the feed rate of the precursor solution as well as the feed distance, and the obtained fiber membrane must subsequently be oxidized at 300 °C and 450 °C in air. In addition, different metal centers have different chemical and electronic properties, and the way one SAC is synthesized cannot be simply extended to another SAC. The comprehensive exploration of SACs has been significantly restricted by the absence of efficient and widely applicable synthetic methodologies.

To overcome these challenges, we propose here a simple and energy-efficient salt-template method to prepare a series of electrocatalysts consisting of 3d-transition metal oxides doped with atomically dispersed noble metals. The atomic ratios of noble metals are around 0.93–3.44%. In this way, it can be said that the performance of the catalysts increases and therefore contributes to significantly reduced cost to meet the requirements of practical

applications. The catalyst represented by Co<sub>3</sub>O<sub>4</sub> doped with Ir (Ir–Co<sub>3</sub>O<sub>4</sub>) shows excellent OER performance over a wide pH range (acidic, alkaline, as well as neutral electrolytes). Particularly, in 0.5 M H<sub>2</sub>SO<sub>4</sub> solution, Ir–Co<sub>3</sub>O<sub>4</sub> exhibits an ultra-low overpotential of 268 mV, at a current density of 10 mA cm<sup>–2</sup>, along with a remarkably low Tafel slope of 38.0 mV dec<sup>–1</sup>, and can operate stably for 16 h at 10 mA cm<sup>–2</sup>, which are far superior to those of commercial IrO<sub>2</sub>, undoped Co<sub>3</sub>O<sub>4</sub>, and most recently reported Ir-based OER electrocatalysts. This work not only establishes a facile synthesis route for SACs, but also highlights their potential as high-performance and cost-effective electrocatalysts for OER applications.

## Results and discussion

3d-transition metal oxides doped with noble metals (NM-TMOs) were synthesized by the salt-template method. First, noble metal precursors and 3d-transition metal precursors were mixed with KCl. Then, NM-TMOs grown on the salt template were obtained by calcination in air. After dissolving the template salt in water, we obtained the NM-TMO materials with high purity and high quality. In this process, the salt crystals act as templates to guide the growth of the oxides at high temperatures, so that the oxides are deposited on this template, which can endow these crystals with a great abundance of edges, corners, and surfaces, and yield oxides with large lateral dimensions.<sup>61</sup> Salt templates can provide electrocatalysts with a large specific surface area and abundant active sites. These active sites are fully exposed on the surface of these oxides, which is conducive to improving the OER performance of the electrocatalysts.<sup>62</sup> This synthesis method is very simple and energy-saving. To further extend the applicability of the synthetic method, a series of NM-TMO electrocatalysts were efficiently prepared by introducing the desired noble metal precursors and 3d-transition metal precursors.

First, using Co<sub>3</sub>O<sub>4</sub> as substrate and varying the noble metal precursors, Ir–Co<sub>3</sub>O<sub>4</sub>, Ru–Co<sub>3</sub>O<sub>4</sub>, and Pd–Co<sub>3</sub>O<sub>4</sub> were synthesized, Fig. 1(a, e and i). The crystal structures of NM-TMOs and control samples are confirmed by X-ray diffraction (XRD). Diffraction peaks appear at 18.8°, 31.1°, 36.7°, 38.4°, 44.7°, 55.6°, 59.3°, and 65.1°, Fig. S1a (ESI†), belonging to the (111), (220), (311), (222), (400), (422), (511) and (440) crystalline planes of Co<sub>3</sub>O<sub>4</sub> (face-centered cubic structure, JCPDS #42-1467), respectively. The XRD patterns of Ir–Co<sub>3</sub>O<sub>4</sub>, Ru–Co<sub>3</sub>O<sub>4</sub>, and Pd–Co<sub>3</sub>O<sub>4</sub> show a standard cubic phase of Co<sub>3</sub>O<sub>4</sub> with good crystallinity, and none of the diffraction peaks are associated with Ir or IrO<sub>2</sub>, Ru or RuO<sub>2</sub>, Pd or PdO, respectively.<sup>63</sup> This result indicates that the crystal structure of Co<sub>3</sub>O<sub>4</sub> remains unaltered by the presence of a small amount of Ir dopant, and further confirms that Ir is in the form of dispersed atoms. The high-resolution transmission electron microscopy (HR-TEM) image of Ir–Co<sub>3</sub>O<sub>4</sub>, Fig. 1b, shows the lattice fringes with a spacing of 0.488 nm, which is larger compared to the (111) facet of Co<sub>3</sub>O<sub>4</sub> (0.467 nm). Moreover, no lattice fringes corresponding to metallic Ir or oxidized Ir nanoparticles are observed. The result indicates that Ir atoms are homogeneously dispersed in the Co<sub>3</sub>O<sub>4</sub> lattice. Similarly, compared to the *d*-spacing of the (220)



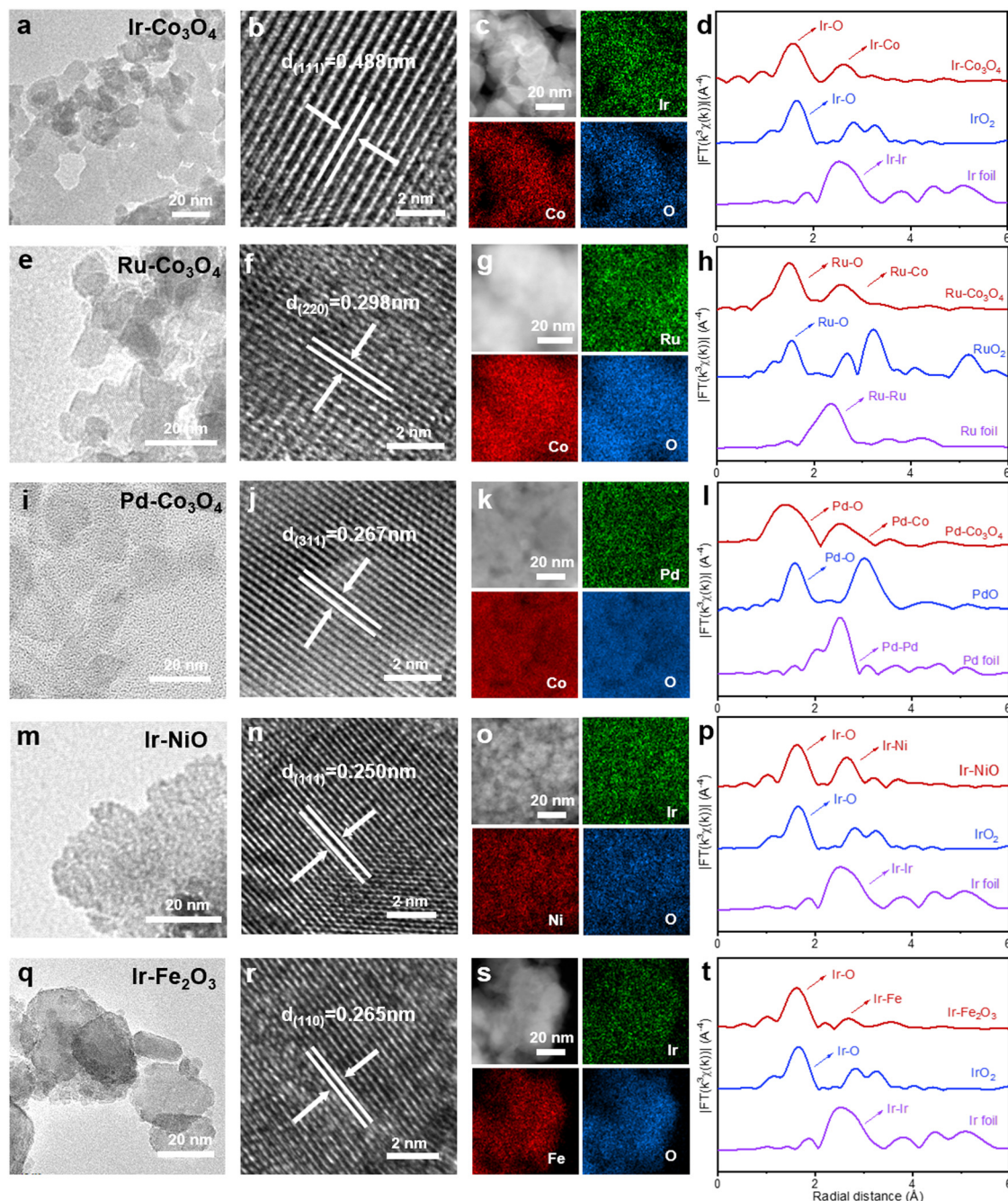


**Fig. 1** (a), (e), (i), (m) and (q) TEM images, (b), (f), (j), (n) and (r) HR-TEM images, (c), (g), (k), (o) and (s) HAADF-STEM images and the corresponding EDS elemental mappings, and EXAFS spectra of (d) Ir-L<sub>3</sub> edge, (h) Ru-K edge, (l) Pd-K edge, (p) Ir-L<sub>3</sub> edge, (t) Ir-L<sub>3</sub> edge for Ir-Co<sub>3</sub>O<sub>4</sub>, Ru-Co<sub>3</sub>O<sub>4</sub>, Pd-Co<sub>3</sub>O<sub>4</sub>, Ir-NiO, and Ir-Fe<sub>2</sub>O<sub>3</sub>, respectively.

planes of Co<sub>3</sub>O<sub>4</sub> (0.286 nm), the *d*-spacing of Ru-Co<sub>3</sub>O<sub>4</sub> (0.298 nm) is larger, Fig. 1f. The *d*-spacing of (311) planes, of Pd-Co<sub>3</sub>O<sub>4</sub> (0.267 nm), is also larger than that of Co<sub>3</sub>O<sub>4</sub> (0.244 nm), Fig. 1j. Furthermore, by changing the transition metal precursors and using the Ir source, Ir-NiO and Ir-Fe<sub>2</sub>O<sub>3</sub> can be synthesized by the same approach, Fig. 1(m and q). After doping with Ir atoms, the *d*-spacings of the (111) planes of Ir-NiO and the *d*-spacings of the (110) planes of Ir-Fe<sub>2</sub>O<sub>3</sub> increase compared to NiO and Fe<sub>2</sub>O<sub>3</sub>, respectively, Fig. 1(n and r). The XRD patterns of Ir-NiO and

Ir-Fe<sub>2</sub>O<sub>3</sub> can be assigned to NiO and Fe<sub>2</sub>O<sub>3</sub>, respectively, in which diffraction peaks for neither Ir nor IrO<sub>2</sub> crystals can be detected, Fig. S1b (ESI†). The uniform spatial distribution of noble metal elements, 3d-transition metal elements, and oxygen in Ir-Co<sub>3</sub>O<sub>4</sub>, Ru-Co<sub>3</sub>O<sub>4</sub>, Pd-Co<sub>3</sub>O<sub>4</sub>, Ir-NiO, and Ir-Fe<sub>2</sub>O<sub>3</sub> can also be confirmed by elemental mappings by energy-dispersive spectroscopy (EDS), Fig. 1(c, g, k, o and s).

In addition, we performed extended X-ray absorption fine structure (EXAFS) analyses to gain insight into the localized





structures of NM-TMOs. The Fourier transformed-EXAFS (FT-EXAFS) spectrum of the Ir-L<sub>3</sub> edge for Ir-Co<sub>3</sub>O<sub>4</sub> displays two prominent peaks in R-space, denoting the first and second coordination shells of the central Ir atom, Fig. 1d. The main peak at about 1.56 Å corresponds to the Ir-O bond, compared to the Ir-O bond of IrO<sub>2</sub> (1.66 Å). The second main peak of the Ir-Co (2.61 Å) bond is much smaller than the Ir-Ir bond in IrO<sub>2</sub> (3.25 Å). The large reduced distance of the second shell originates from an edge-sharing network in Co<sub>3</sub>O<sub>4</sub> as compared with a corner-sharing network in IrO<sub>2</sub>.<sup>64</sup> The k<sup>3</sup>-weighted EXAFS spectrum of Ir-L<sub>3</sub> was analyzed by wavelet transform, in Fig. S2(a-c) (ESI†). The wavelet transforms intensity maximum around 6.70 Å<sup>-1</sup> arising from the Ir-O coordination is well resolved at 1.59 Å for Ir-Co<sub>3</sub>O<sub>4</sub>, which is similar to the Ir-O coordination in IrO<sub>2</sub>, while an intensity maximum at about 10.95 Å<sup>-1</sup> associated with the Ir-Ir coordination in Ir foil is not

observed in Ir-Co<sub>3</sub>O<sub>4</sub>.<sup>65</sup> These results show that Ir-Ir scattering is absent in Ir-Co<sub>3</sub>O<sub>4</sub> and, therefore, the formation of Ir cluster can be excluded. Similarly, FT-EXAFS spectra demonstrate that the noble metal species in Ru-Co<sub>3</sub>O<sub>4</sub>, Pd-Co<sub>3</sub>O<sub>4</sub>, Ir-NiO, and Ir-Fe<sub>2</sub>O<sub>3</sub> are present as single atoms, Fig. 1(h, l, p and t) and Fig. S2(d-o) (ESI†). In summary, all catalysts showed a nano-particular structure. Subsequent analysis of HR-TEM, EDS elemental mapping, and EXAFS spectra confirmed that the noble metal was uniformly doped into the lattice of the 3d-transition metal oxides in the form of single atoms. Undoubtedly, these characterization results fully confirm the universality of this synthesis method, which can achieve a diverse combination of atomically dispersed noble metals and 3d-transition metal oxides. This simple KCl method of preparing template, as well as the simple and nondestructive green transfer process, are of great importance for research in the

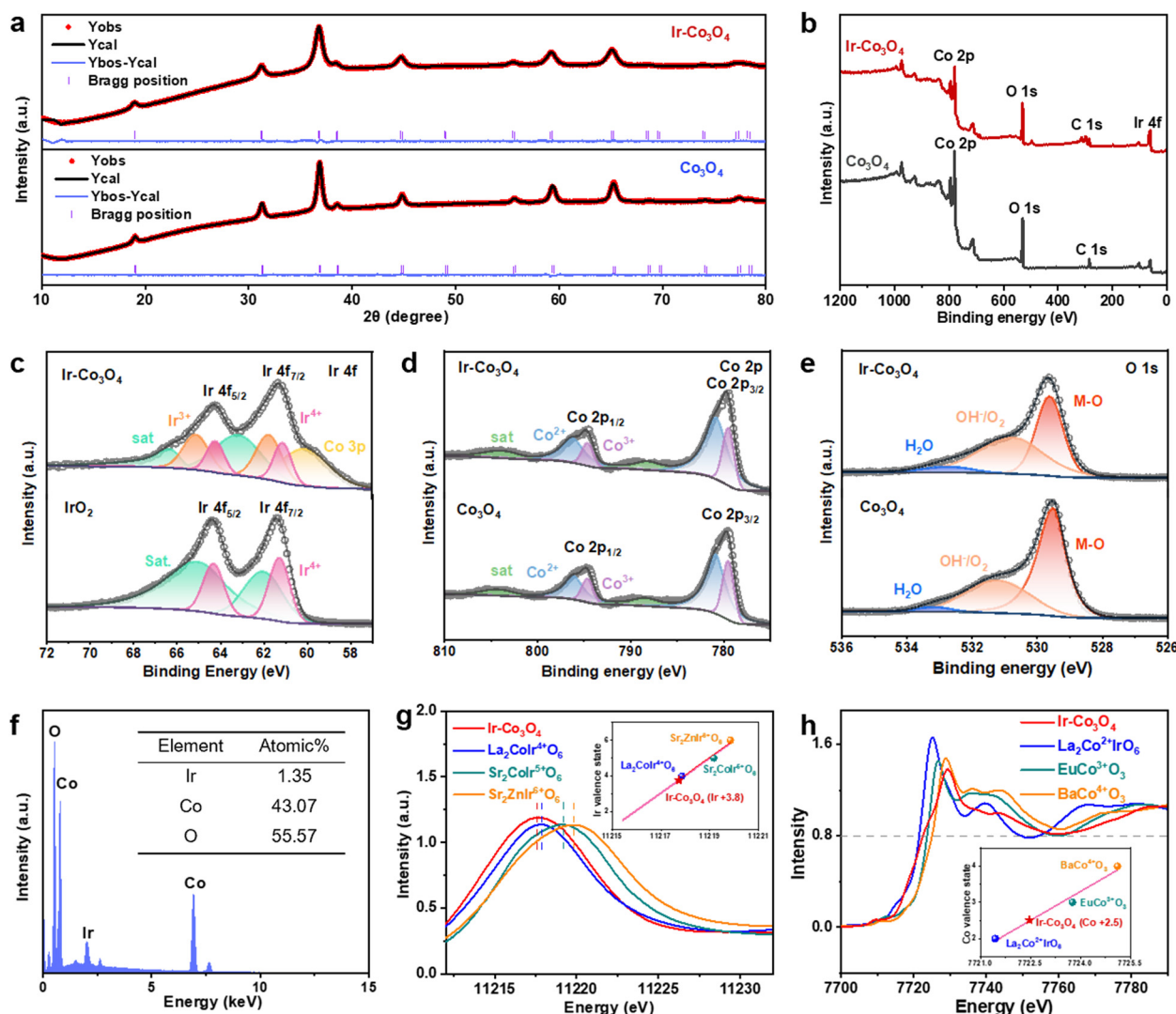


**Fig. 2** (a) Rietveld refinements of XRD patterns for Ir-Co<sub>3</sub>O<sub>4</sub> and Co<sub>3</sub>O<sub>4</sub>. (b) XPS survey spectra of Ir-Co<sub>3</sub>O<sub>4</sub> and Co<sub>3</sub>O<sub>4</sub>. XPS spectra of (c) Ir 4f for Ir-Co<sub>3</sub>O<sub>4</sub> and IrO<sub>2</sub>, (d) Co 2p, and (e) O 1s for Ir-Co<sub>3</sub>O<sub>4</sub> and Co<sub>3</sub>O<sub>4</sub>. (f) SEM-EDS spectrum of Ir-Co<sub>3</sub>O<sub>4</sub>. (g) The normalized XANES spectra of Ir-L<sub>3</sub> edge for Ir-Co<sub>3</sub>O<sub>4</sub>, La<sub>2</sub>CoIr<sup>4+</sup>O<sub>6</sub>, Sr<sub>2</sub>CoIr<sup>5+</sup>O<sub>6</sub>, and Sr<sub>2</sub>ZnIr<sup>6+</sup>O<sub>6</sub>. The inset shows the Ir valence state. (h) The normalized XANES spectra of Co-K edge for Ir-Co<sub>3</sub>O<sub>4</sub>, La<sub>2</sub>Co<sup>2+</sup>IrO<sub>6</sub>, EuCo<sup>3+</sup>O<sub>3</sub>, and BaCo<sup>4+</sup>O<sub>3</sub>. The inset shows the Co valence state.

preparation of single-atom noble metal doped TMO batches and the exploration of industrial applications.

We further investigated the structural and electronic properties of NM-TMO materials prepared by this method using Ir-Co<sub>3</sub>O<sub>4</sub> as an example. XRD patterns of Ir-Co<sub>3</sub>O<sub>4</sub> and undoped Co<sub>3</sub>O<sub>4</sub> samples were refined, Fig. 2a and Table S1 (ESI<sup>†</sup>). The results showed that the lattice constant of Ir-Co<sub>3</sub>O<sub>4</sub> ( $a = b = c = 8.10224$  Å) increased after Ir doping compared to that of Co<sub>3</sub>O<sub>4</sub> ( $a = b = c = 8.08579$  Å), indicating that Ir was successfully dispersed into the Co<sub>3</sub>O<sub>4</sub> lattice, causing the Co<sub>3</sub>O<sub>4</sub> lattice to expand, Table S2 (ESI<sup>†</sup>). This result agrees with the HR-TEM results of Ir-Co<sub>3</sub>O<sub>4</sub> mentioned above, Fig. 1c. The surface chemical states of the prepared materials were analyzed by X-ray photoelectron spectroscopy (XPS). The full XPS survey spectrum of Ir-Co<sub>3</sub>O<sub>4</sub> confirms that Ir, Co, and O are present on the surface, Fig. 2b, which is in agreement with previous EDS mappings. Analyzing the high-resolution XPS spectra, Fig. 2c, the Ir 4f spectrum of commercial IrO<sub>2</sub> shows a set of double peaks at 61.3 eV and 64.3 eV, which can be attributed to Ir<sup>4+</sup>. For Ir-Co<sub>3</sub>O<sub>4</sub>, the peak at about 60.1 eV corresponds to Co 3p, and the Ir 4f spectrum reveals two sets of double peaks, centered at 61.1/64.2 eV and 61.7/65.1 eV, and attributed to Ir<sup>4+</sup> and Ir<sup>3+</sup>, respectively.<sup>65,66</sup> The Co 2p spectra of Co<sub>3</sub>O<sub>4</sub> and Ir-Co<sub>3</sub>O<sub>4</sub> contain Co<sup>2+</sup>, Co<sup>3+</sup>, and satellite peaks, Fig. 2d. The Co<sup>2+</sup> peaks are located at 796.1 eV (2p<sub>1/2</sub>) and 780.9 eV (2p<sub>3/2</sub>), and the Co<sup>3+</sup> peaks are located at 794.6 eV (2p<sub>1/2</sub>) and 779.5 eV (2p<sub>3/2</sub>).<sup>22,60</sup> The increase in the Co<sup>2+</sup> to Co<sup>3+</sup> ratio after Ir doping in Co<sub>3</sub>O<sub>4</sub> indicates that Ir atoms replace Co<sup>3+</sup> atoms at the octahedral sites, leading to the formation of more Co<sup>2+</sup> to balance the surface oxygen vacancies.<sup>67</sup> The chemical state of O 1s in Co<sub>3</sub>O<sub>4</sub> and Ir-Co<sub>3</sub>O<sub>4</sub> shows three peaks including lattice oxygen (M-O) at 529.5 eV, hydroxyl and oxygen vacancies (OH<sup>-</sup>/O<sub>2</sub>) at 531.2 eV, and adsorbed water molecules (H<sub>2</sub>O) at 532.8 eV, Fig. 2e.<sup>22</sup> With Ir doping, the proportion of absorbed oxygen increases compared to lattice oxygen, suggesting that doping produces a large number of oxygen vacancies, providing more catalytically active sites.<sup>67</sup>

The remaining NM-TMOs and their corresponding undoped TMOs were also analyzed by XPS to obtain the surface chemistry and valence states of the metal elements and oxygen, Fig. S3 (ESI<sup>†</sup>). The binding energies of Ru 3p<sub>1/2</sub> and 3p<sub>3/2</sub> at 487.3 eV and 465.3 eV suggest that Ru in Ru-Co<sub>3</sub>O<sub>4</sub> occurs as Ru<sup>4+</sup>. Upon doping in Co<sub>3</sub>O<sub>4</sub>, the binding energy of Ru shifts about 1.0 eV for Ru 3p compared to RuO<sub>2</sub>, revealing a significant change in the electronic structure due to the doping effect, Fig. S3(a and d) (ESI<sup>†</sup>). In Pd-Co<sub>3</sub>O<sub>4</sub>, the deconvoluted spectrum of Pd 3d shows two sets of double peaks located at 336.7/342.0 eV and 338.4/343.9 eV, which are assigned to Pd<sup>2+</sup> and Pd<sup>4+</sup>, respectively, Fig. S3(g and j) (ESI<sup>†</sup>).<sup>54</sup> The binding energy level of Pd 3d after doping in Co<sub>3</sub>O<sub>4</sub> is shifted by about 0.3 eV, compared to that of PdO. When Co<sub>3</sub>O<sub>4</sub> were doped with Ru and Pd, the ratio of Co<sup>2+</sup> also increased compared to that of Co<sup>3+</sup>, Fig. S3(b, e, h and k) (ESI<sup>†</sup>), suggesting that noble metal atoms replaced the octahedral sites of Co<sup>3+</sup>, resulting in the formation of more Co<sup>2+</sup> to balance the surface oxygen vacancies. The O 1s spectra of all four materials show a higher proportion of absorbed oxygen

compared to lattice oxygen, Fig. S3(c, f, i, l, o, r, u and x) (ESI<sup>†</sup>). Quantitative analysis of the SEM-EDS element spectra shows that Ir-Co<sub>3</sub>O<sub>4</sub> contains 1.35 at% of Ir, Fig. 2f. For other NM-TMO materials, Ru-Co<sub>3</sub>O<sub>4</sub> contains 1.4 at% of Ru, Pd-Co<sub>3</sub>O<sub>4</sub> contains 0.9 at% of Pd, Ir-NiO contains 3.4 at% of Ir, and Ir-Fe<sub>2</sub>O<sub>3</sub> contains 1.6 at% of Ir, Fig. S4(a-d) (ESI<sup>†</sup>). The above results are averages of multiple measurements and mostly consistent with the elemental content of the surface layer determined by XPS, Table S3 (ESI<sup>†</sup>).

The electronic structure of Ir-Co<sub>3</sub>O<sub>4</sub> is further analyzed using the Ir-L<sub>3</sub> X-ray absorption near edge structure (XANES) spectrum. Fig. 2g shows Ir-L<sub>3</sub> XANES of Ir-Co<sub>3</sub>O<sub>4</sub> together with La<sub>2</sub>CoIr<sup>4+</sup>O<sub>6</sub>, Sr<sub>2</sub>CoIr<sup>5+</sup>O<sub>6</sub>, and Sr<sub>2</sub>ZnIr<sup>6+</sup>O<sub>6</sub> for comparison. We obtained the valence state of Ir<sup>3.8+</sup> in Ir-Co<sub>3</sub>O<sub>4</sub> (inset, Fig. 2g). Based on the relationship between the absorption edge energy positions (at 0.8 normalized intensity), the XANES spectra of Co K in Ir-Co<sub>3</sub>O<sub>4</sub> and in La<sub>2</sub>Co<sup>2+</sup>IrO<sub>6</sub>, EuCo<sup>3+</sup>O<sub>3</sub>, and BaCo<sup>4+</sup>O<sub>3</sub> are presented in Fig. 2h, the estimated valence state of the Co ion in Ir-Co<sub>3</sub>O<sub>4</sub>, is about +2.5 (inset, Fig. 2h). The corresponding K-edge EXAFS of Co shows three main signals associated with the Co-O, Co-Co<sub>oct</sub> (octahedral site), and Co-Co<sub>tet</sub> (tetrahedral site) scattering paths, Fig. S5 (ESI<sup>†</sup>). These results are in good agreement with the XPS results.

The valences of Ir, Ru, and Pd are determined by Ir foil and IrO<sub>2</sub> references, Ru foil and RuO<sub>2</sub> references, Pd foil and PdO references, respectively. The white line peak position of the Ir-L<sub>3</sub> edge in Ir-NiO and Ir-Fe<sub>2</sub>O<sub>3</sub> is between those for Ir foil and IrO<sub>2</sub>, indicating that the Ir has a valence state between 0 to +4. Similarly, the oxidation state of Ru in the Ru-Co<sub>3</sub>O<sub>4</sub> and Pd in Pd-Co<sub>3</sub>O<sub>4</sub> is between 0 to +4 and 0 to +2, according to their energy position of absorption edge at the Ru- and Pd-K XANES spectra in Fig. S6(a-d), ESI<sup>†</sup>.

We evaluated the electrocatalytic OER performance of the representative Ir-Co<sub>3</sub>O<sub>4</sub> sample using a standard three-electrode system in three different electrolyte solutions, *i.e.*, 0.5 M H<sub>2</sub>SO<sub>4</sub>, 1.0 M KOH, and 1 × PBS solutions. All measurements were performed with 95% *iR* compensation, and the measured potentials were calibrated according to the reversible hydrogen electrode (RHE). Commercial IrO<sub>2</sub> catalyst and undoped Co<sub>3</sub>O<sub>4</sub> were used as references. First, we tested and discussed the performance of each catalyst in the acidic electrolyte (0.5 M H<sub>2</sub>SO<sub>4</sub> solution). The linear scanning voltammetry (LSV) curves shown in Fig. 3a were recorded on a glassy carbon electrode (GCE) with a geometric area of 0.196 cm<sup>2</sup>. At the current density of 10 mA cm<sup>-2</sup>, Ir-Co<sub>3</sub>O<sub>4</sub> showed an overpotential of 268 mV, which is lower than that of Co<sub>3</sub>O<sub>4</sub> (466 mV) and commercial IrO<sub>2</sub> (329 mV). The acidic OER properties of the catalysts prepared using this synthesis method are shown in Fig. S7(a and b), ESI<sup>†</sup>. These catalysts showed improved performance compared to both commercial IrO<sub>2</sub> and undoped Co<sub>3</sub>O<sub>4</sub>. Among them, the overpotentials of these catalysts at a current density of 10 mA cm<sup>-2</sup> follow the orders: Ir-Co<sub>3</sub>O<sub>4</sub> < Ir-NiO < Ir-Fe<sub>2</sub>O<sub>3</sub> < IrO<sub>2</sub> (Fig. S7a, ESI<sup>†</sup>) and Ir-Co<sub>3</sub>O<sub>4</sub> < Ru-Co<sub>3</sub>O<sub>4</sub> < Pd-Co<sub>3</sub>O<sub>4</sub> < Co<sub>3</sub>O<sub>4</sub> (Fig. S7b, ESI<sup>†</sup>). The above results indicate that the synthesis method is a versatile method for the preparation of noble metal single-atom doped 3d-transition metal oxide electrocatalysts. Tafel plots are used to



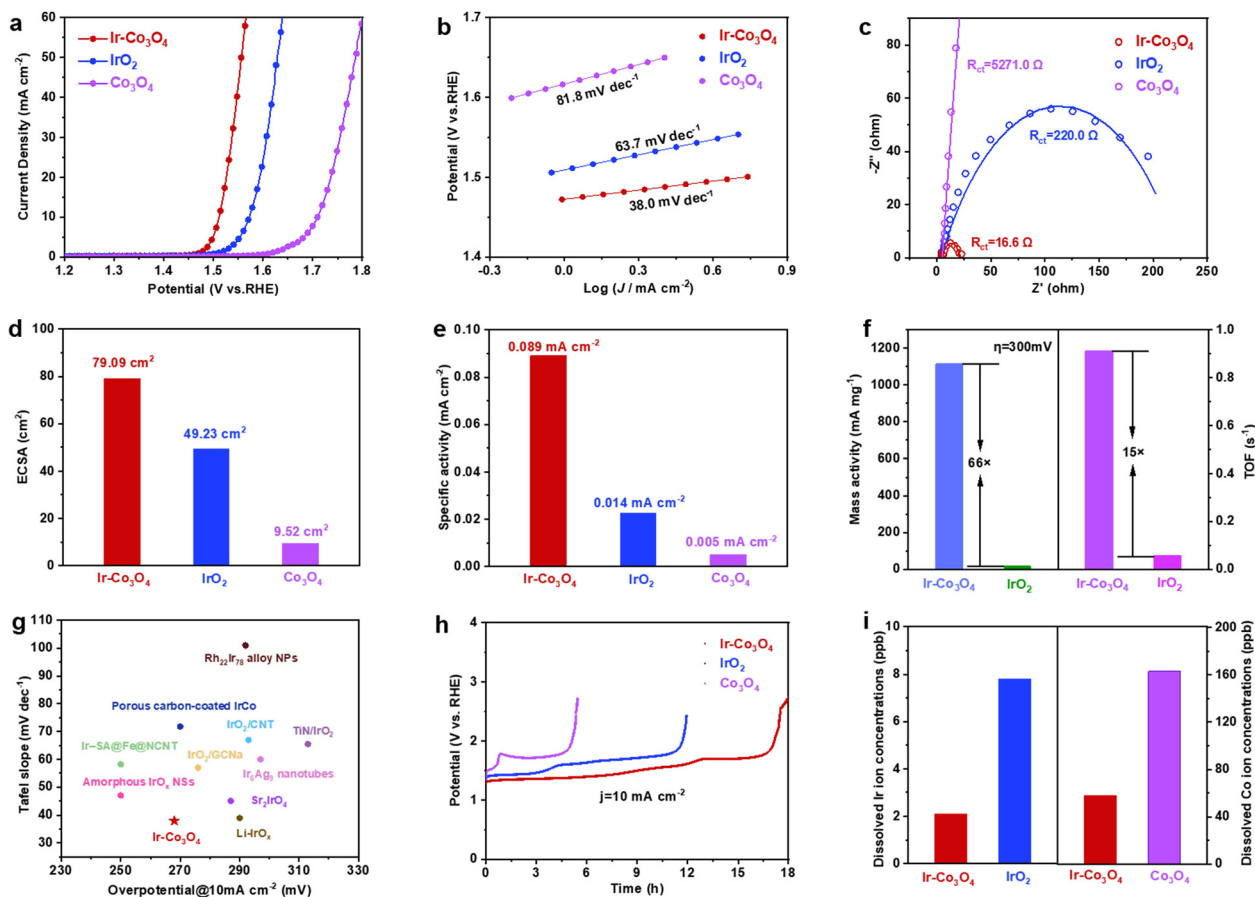


**Fig. 3** (a) LSV curves of Ir–Co<sub>3</sub>O<sub>4</sub>, IrO<sub>2</sub>, and Co<sub>3</sub>O<sub>4</sub> collected at a scanning rate of 5 mV s<sup>−1</sup> in 0.5 M H<sub>2</sub>SO<sub>4</sub> solution. (b) The corresponding Tafel plots were obtained from the polarization curves in (a). (c) Nyquist plots and corresponding fitting curves of the samples obtained at 1.49 V vs. RHE for EIS analysis. (d) The calculated ECSA values for Ir–Co<sub>3</sub>O<sub>4</sub>, IrO<sub>2</sub>, and Co<sub>3</sub>O<sub>4</sub> in 0.5 M H<sub>2</sub>SO<sub>4</sub>. (e) Specific activity of Ir–Co<sub>3</sub>O<sub>4</sub>, IrO<sub>2</sub>, and Co<sub>3</sub>O<sub>4</sub>. (f) Mass activities and TOF values of Ir–Co<sub>3</sub>O<sub>4</sub>, IrO<sub>2</sub> at the overpotential of 300 mV. (g) Comparison of overpotentials at 10 mA cm<sup>−2</sup> and Tafel slopes among reported Ir-based OER electrocatalysts. (h) Chronopotentiometric measurements of Ir–Co<sub>3</sub>O<sub>4</sub>, IrO<sub>2</sub>, and Co<sub>3</sub>O<sub>4</sub> at 10 mA cm<sup>−2</sup>. (i) Dissolved Ir and Co (left and right y-axis, respectively) ion concentrations in the electrolyte measured by ICP-OES for Ir–Co<sub>3</sub>O<sub>4</sub>, IrO<sub>2</sub>, and Co<sub>3</sub>O<sub>4</sub>.

evaluate the kinetic behavior of the electrocatalysts, Fig. 3b, and show slopes of 38.0, 63.7, and 81.8 mV dec<sup>−1</sup> for Ir–Co<sub>3</sub>O<sub>4</sub>, commercial IrO<sub>2</sub>, and Co<sub>3</sub>O<sub>4</sub> catalysts, respectively, reflecting the fastest reaction rate for the Ir–Co<sub>3</sub>O<sub>4</sub> catalysts, and indicating that the Ir doping could promote the OER kinetics. Electrochemical impedance spectroscopy (EIS) is a commonly used technique to understand OER activity. As shown in Fig. 3c, Ir–Co<sub>3</sub>O<sub>4</sub> has a much smaller charge transfer resistance ( $R_{ct}$ ) (16.6  $\Omega$ ) compared to commercial IrO<sub>2</sub> (220.0  $\Omega$ ) and Co<sub>3</sub>O<sub>4</sub> (5271.0  $\Omega$ ) values deduced from an equivalent circuit (Fig. S8, ESI<sup>†</sup>), revealing the fast electron transfer of Ir–Co<sub>3</sub>O<sub>4</sub> during the OER reaction (Table S4, ESI<sup>†</sup>). Fig. S9 (ESI<sup>†</sup>) shows the TEM image of Co<sub>3</sub>O<sub>4</sub>, which demonstrates that Co<sub>3</sub>O<sub>4</sub> has a similar morphology to Ir–Co<sub>3</sub>O<sub>4</sub> (Fig. 1a), so the differences in catalytic performance are not due to morphology or size disparities. The charge density difference on Ir–Co<sub>3</sub>O<sub>4</sub> indicates that incorporation of Ir into Co<sub>3</sub>O<sub>4</sub> can effectively regulate charge redistribution, where Ir atoms tend to lose electrons and off-domain electrons accumulate around neighboring Ir–O bonds. This result also confirms the existence of strong electronic interactions between Ir single sites and the host Co<sub>3</sub>O<sub>4</sub>. The introduction of Ir single atoms endows Co<sub>3</sub>O<sub>4</sub> with metallic

properties, leading to better electrical conductivity and thus faster OER dynamics. Stronger interactions and more covalent properties between Co and Ir atoms suggest synergistic effects between Ir atoms and Co<sub>3</sub>O<sub>4</sub>.<sup>65</sup>

In addition, cyclic voltammetry (CV) scans, at different scan rates, were performed to measure the electrochemical double-layer capacitance ( $C_{dl}$ ), which was used to calculate the effective electrochemical surface area (ECSA), Fig. S10(a–d), ESI<sup>†</sup>. It can be seen that the ECSA of Ir–Co<sub>3</sub>O<sub>4</sub> is 79.09 cm<sup>2</sup>, much higher than that of commercial IrO<sub>2</sub> (49.23 cm<sup>2</sup>), as well as that of Co<sub>3</sub>O<sub>4</sub> (9.52 cm<sup>2</sup>), Fig. 3d. To further investigate the intrinsic activity of the catalyst, the specific activity of Ir–Co<sub>3</sub>O<sub>4</sub>, IrO<sub>2</sub>, and Co<sub>3</sub>O<sub>4</sub> is determined by normalizing the catalytic current to the ECSA of the catalysts. At an overpotential ( $\eta$ ) of 300 mV, Ir–Co<sub>3</sub>O<sub>4</sub> exhibits the highest specific activity (0.089 mA cm<sub>ECSA</sub><sup>−2</sup>), which exceeds the specific activities of IrO<sub>2</sub> (0.014 mA cm<sub>ECSA</sub><sup>−2</sup>) and Co<sub>3</sub>O<sub>4</sub> (0.005 mA cm<sub>ECSA</sub><sup>−2</sup>) by approximately 6.4 and 17.8 times, respectively, Fig. 3e. As shown in Fig. 3f, Ir–Co<sub>3</sub>O<sub>4</sub> has 66 times higher mass activity (MA) as well as 15 times higher turnover frequency (TOF) than that of commercial IrO<sub>2</sub> at  $\eta$  = 300 mV. The above results suggest that the doping with Ir contributes to a

significant increase in the utilization of Ir atoms as well as the active sites of the  $\text{Co}_3\text{O}_4$  catalyst, thus improving its intrinsic activity. It is noteworthy that the overpotential of  $\text{Ir-Co}_3\text{O}_4$  catalyst at  $10 \text{ mA cm}^{-2}$  and its Tafel slope in acidic electrolyte ( $0.5 \text{ M H}_2\text{SO}_4$ ) is lower than those of most Ir-based OER catalysts, Fig. 3g and Table S5 (ESI<sup>†</sup>).

Apart from activity, the durability of OER electrocatalysts is also a crucial parameter to evaluate their performance.  $\text{Ir-Co}_3\text{O}_4$  demonstrates stability over 16 h at a current density of  $10 \text{ mA cm}^{-2}$ , exceeding that of commercial  $\text{IrO}_2$  and  $\text{Co}_3\text{O}_4$  and showing the lowest degradation of its OER activity, Fig. 3h. This suggests that doping a small amount of Ir can obviously improve the stability of  $\text{Co}_3\text{O}_4$ .<sup>68</sup> Nevertheless,  $\text{Ir-Co}_3\text{O}_4$  still has some limitations due to the intrinsic instability of  $\text{Co}_3\text{O}_4$  under harsh OER conditions (e.g. oxidation potentials; acidic electrolytes).<sup>65</sup> Following the OER stability test, inductively coupled plasma-atomic emission spectrometry (ICP-OES) measurement showed severe leaching of Ir ions in  $\text{IrO}_2$  and Co ions in  $\text{Co}_3\text{O}_4$  compared to  $\text{Ir-Co}_3\text{O}_4$ , Fig. 3i. The inhibitory

effect of Ir-doped  $\text{Co}_3\text{O}_4$  on the dissolution of Ir ions and Co ions is illustrated, which further explains the higher stability of the  $\text{Ir-Co}_3\text{O}_4$  catalyst. Morphological characterization by low-magnification TEM shows that  $\text{Ir-Co}_3\text{O}_4$  retains nanoparticles after chronopotentiometric measurement at  $10 \text{ mA cm}^{-2}$ , Fig. S11a (ESI<sup>†</sup>), and the HR-TEM image shows no obvious structural changes, Fig. S11b (ESI<sup>†</sup>). EDS elemental mappings show that the distribution of Co, Ir, and O elements, after the stability test, remained uniform throughout  $\text{Ir-Co}_3\text{O}_4$ , Fig. S11c (ESI<sup>†</sup>). However, the XPS spectra of Ir 4f and Co 2p show an increase in the valence of Ir and Co after chronopotentiometry of  $\text{Ir-Co}_3\text{O}_4$  at  $10 \text{ mA cm}^{-2}$ , which is common in OER catalysts at oxidizing applied electrode potentials, Fig. S11(d and e) (ESI<sup>†</sup>). The XPS spectrum of O 1s shows an increase in the proportion of absorbed oxygen, providing further confirmation of the increase in the overall catalyst valence after the stability test, Fig. S11f (ESI<sup>†</sup>).

Next, the electrochemical performance of each catalyst in the alkaline electrolyte ( $1.0 \text{ M KOH}$  solution) is analyzed. In the

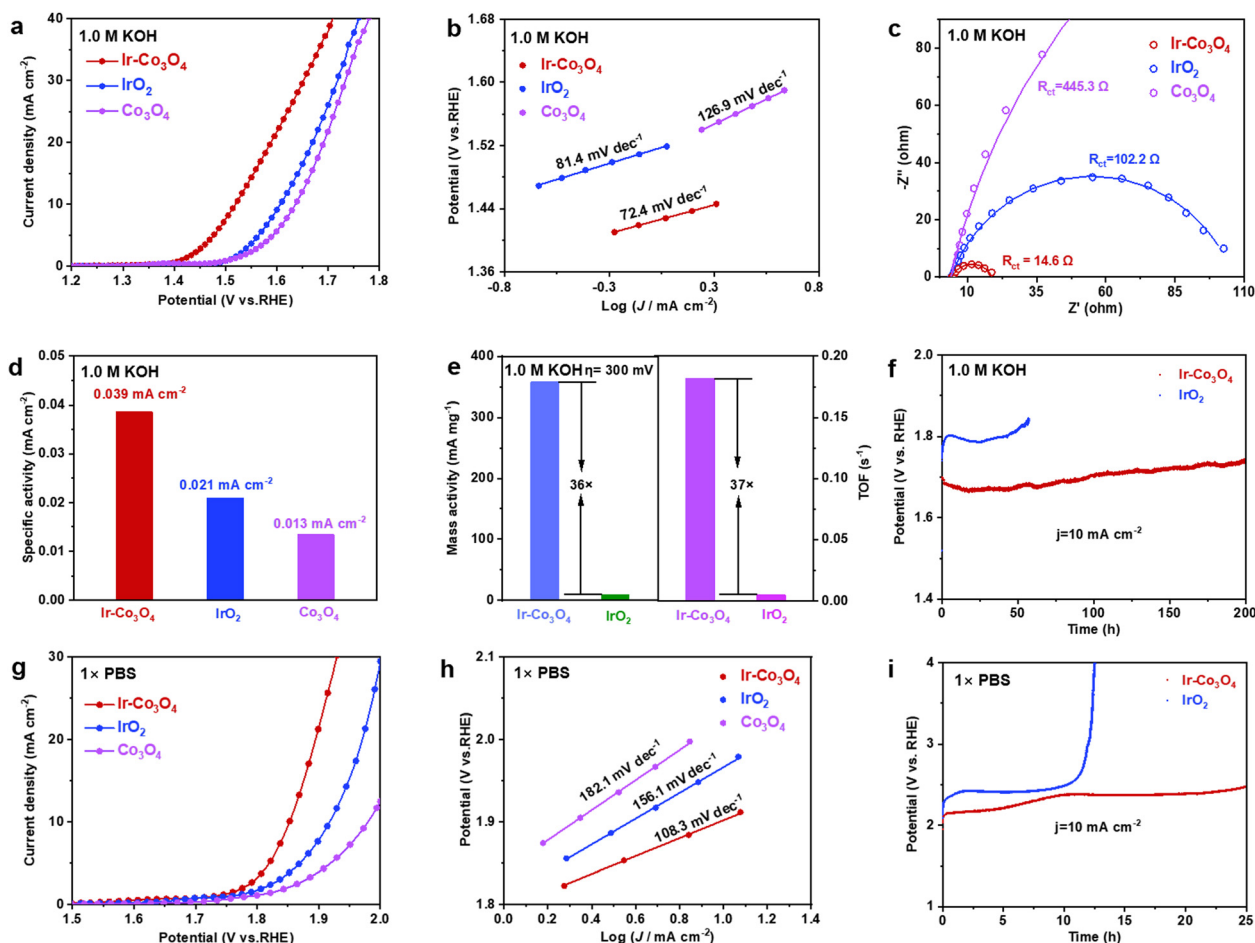


**Fig. 4** (a) LSV curves of  $\text{Ir-Co}_3\text{O}_4$ ,  $\text{IrO}_2$ , and  $\text{Co}_3\text{O}_4$  in  $1.0 \text{ M KOH}$  at a scanning rate of  $5 \text{ mV s}^{-1}$ . (b) The corresponding Tafel plots were obtained from the polarization curves in (a). (c) Nyquist plots and corresponding fitting curves of samples obtained at  $1.52 \text{ V vs. RHE}$ . (d) Specific activity of  $\text{Ir-Co}_3\text{O}_4$ ,  $\text{IrO}_2$ , and  $\text{Co}_3\text{O}_4$ . (e) Mass activities and TOF values of  $\text{Ir-Co}_3\text{O}_4$  and  $\text{IrO}_2$  at  $300 \text{ mV}$  overpotential. (f) Chronopotentiometric measurements, in  $1.0 \text{ M KOH}$ , of  $\text{Ir-Co}_3\text{O}_4$  and  $\text{IrO}_2$  at  $10 \text{ mA cm}^{-2}$  using carbon paper as catalyst support. (g) LSV curves of  $\text{Ir-Co}_3\text{O}_4$ ,  $\text{IrO}_2$ , and  $\text{Co}_3\text{O}_4$  in  $1 \times \text{PBS}$  at a scanning rate of  $5 \text{ mV s}^{-1}$ . (h) The corresponding Tafel plots were obtained from the LSV curves in (g). (i) Chronopotentiometric measurements, in  $1 \times \text{PBS}$ , of  $\text{Ir-Co}_3\text{O}_4$  and  $\text{IrO}_2$  at  $10 \text{ mA cm}^{-2}$ .



LSV curves, Fig. 4a, Ir-Co<sub>3</sub>O<sub>4</sub> has a lower overpotential (289 mV) at 10 mA cm<sup>-2</sup>, compared to IrO<sub>2</sub> (377 mV) and Co<sub>3</sub>O<sub>4</sub> (406 mV), demonstrating a good OER activity of Ir-Co<sub>3</sub>O<sub>4</sub> in alkaline electrolyte. The Tafel slopes of Ir-Co<sub>3</sub>O<sub>4</sub>, commercial IrO<sub>2</sub>, and Co<sub>3</sub>O<sub>4</sub> catalysts are 72.4, 81.4, and 126.9 mV dec<sup>-1</sup>, respectively, Fig. 4b. The lower Tafel slope of Ir-Co<sub>3</sub>O<sub>4</sub> suggests that it has a higher reaction rate than commercial IrO<sub>2</sub> and Co<sub>3</sub>O<sub>4</sub> catalysts. In the EIS Nyquist plot displayed in Fig. 4c, the interfacial charge transfer resistance of Ir-Co<sub>3</sub>O<sub>4</sub> (14.6 Ω) was reduced compared with that of IrO<sub>2</sub> (102.2 Ω) and Co<sub>3</sub>O<sub>4</sub> (445.3 Ω) (Table S6, ESI<sup>†</sup>), indicating that the doping of the noble metal Ir led to a decrease of the electron conduction activation energy, which improved the conductivity of the catalysts, thus promoting the catalytic activity. The ECSA of Ir-Co<sub>3</sub>O<sub>4</sub>, 58.52 cm<sup>2</sup>, was higher than that of IrO<sub>2</sub> (20.44 cm<sup>2</sup>) and Co<sub>3</sub>O<sub>4</sub> (24.04 cm<sup>2</sup>), Fig. S12(a-e) (ESI<sup>†</sup>). By normalizing the OER current to ECSA at η = 300 mV, Ir-Co<sub>3</sub>O<sub>4</sub> exhibits higher specific activity (0.039 mA cm<sub>ECSA</sub><sup>-2</sup>) than the commercial IrO<sub>2</sub> (0.021 mA cm<sub>ECSA</sub><sup>-2</sup>) and Co<sub>3</sub>O<sub>4</sub> (0.013 mA cm<sub>ECSA</sub><sup>-2</sup>), Fig. 4d. In addition, the MA and TOF were calculated at η = 300 mV, Fig. 4e. Ir-Co<sub>3</sub>O<sub>4</sub> showed a MA (358.0 mA mg<sup>-1</sup>) 36 times higher than that of IrO<sub>2</sub> (9.9 mA mg<sup>-1</sup>), and a TOF (0.1821 s<sup>-1</sup>) 37 times higher than that of IrO<sub>2</sub> (0.0049 s<sup>-1</sup>). The above results showed that Ir doping also greatly enhances the catalytic activity of Co<sub>3</sub>O<sub>4</sub> in alkaline electrolytes, and its activity is superior to that of IrO<sub>2</sub> with the same mass loading. Meanwhile, Ir-Co<sub>3</sub>O<sub>4</sub> also shows better stability than IrO<sub>2</sub>, Fig. 4f. Ir-Co<sub>3</sub>O<sub>4</sub> can operate stably for 200 h at 10 mA cm<sup>-2</sup> and the potential only increased slightly by 0.08 V, while the IrO<sub>2</sub> catalyst was deactivated after only 44 h. This reflects that Ir doping in Co<sub>3</sub>O<sub>4</sub> can substantially improve the durability of Ir-based catalysts.

To better understand the electrochemical performance of the Ir-Co<sub>3</sub>O<sub>4</sub> catalyst over the entire pH range, we tested the OER performance in 1 × PBS neutral electrolyte. As shown in Fig. 4(g and h), the overpotential of Ir-Co<sub>3</sub>O<sub>4</sub> at current density = 10 mA cm<sup>-2</sup> (622 mV) was lower than that of IrO<sub>2</sub> (687 mV) and Co<sub>3</sub>O<sub>4</sub> (749 mV), and the Tafel slope of Ir-Co<sub>3</sub>O<sub>4</sub> (108.3 mV dec<sup>-1</sup>) was the lowest of the three. This suggests that Ir-Co<sub>3</sub>O<sub>4</sub> has a better catalytic activity compared to IrO<sub>2</sub> and Co<sub>3</sub>O<sub>4</sub> in neutral electrolytes. To investigate the stability in neutral electrolyte, the catalysts were tested for stability under the same conditions at 10 mA cm<sup>-2</sup>. Fig. 4i shows that the Ir-Co<sub>3</sub>O<sub>4</sub> catalyst remained stable for 25 h, while the IrO<sub>2</sub> catalyst started to deactivate after 10 h of testing. These results indicate that Ir-Co<sub>3</sub>O<sub>4</sub> has a long-term durability in neutral electrolyte. The above results suggest that Ir doping significantly improves the OER performance of Co<sub>3</sub>O<sub>4</sub> in acidic, alkaline, and neutral electrolytes.

## Conclusions

In summary, we present a universal salt-template method to prepare 3d-transition metal oxides doped with single noble metal atoms. In addition to Ir-Co<sub>3</sub>O<sub>4</sub>, a wide variety of electrocatalysts, including Ru-Co<sub>3</sub>O<sub>4</sub>, Pd-Co<sub>3</sub>O<sub>4</sub>, Ir-NiO, and Ir-Fe<sub>2</sub>O<sub>3</sub>, can be obtained by simply substituting the noble metal or the 3d-transition metal precursor. EXAFS spectroscopy reveals that

the noble metals in the NM-TMO electrocatalysts synthesized by this method are all in the monoatomic form and uniformly dispersed in the nanoparticles, which greatly enhances the atomic utilization of the noble metals and provides more active sites for the catalysts. Surprisingly, the Ir-Co<sub>3</sub>O<sub>4</sub> synthesized by this method showed excellent electrocatalytic performance and stability compared with commercial IrO<sub>2</sub> and Co<sub>3</sub>O<sub>4</sub> in acidic, alkaline, and neutral media. The present study demonstrates the versatility of the synthesis method over a wide pH range, which not only reduces the catalyst cost by decreasing the precious metals content but also improves the catalytic performance. The simplicity and energy-saving characteristics of the synthesis method will be of great reference value for the practical application of various noble metal-based catalysts.

## Experimental

### Materials

Iridium(III) trichloride (IrCl<sub>3</sub>, solid, 99.9%), cobalt chloride hexahydrate (CoCl<sub>2</sub>·6H<sub>2</sub>O, solid, AR), nickel chloride hexahydrate (NiCl<sub>2</sub>·6H<sub>2</sub>O, solid, 98%), potassium chloride (KCl, solid, ≥99.0%), and sodium hydroxide (NaOH, solid, ≥98%) were purchased from Aladdin. Palladium(II) chloride (PdCl<sub>2</sub>, solid, Pd 59–60%), ruthenium(III) chloride (RuCl<sub>3</sub>, solid, 99.5%), iridium(IV) oxide (IrO<sub>2</sub>, solid, 99.9%), ruthenium dioxide (RuO<sub>2</sub>, solid, 99%), palladium(II) oxide (PdO, solid, 98%), and 1 × phosphate buffered saline (1 × PBS, solution, pH 7.2–7.4, 0.01 M) were purchased from Innochem. Potassium chloride (KCl, solid, 99.8%), iron trichloride hexahydrate (FeCl<sub>3</sub>·6H<sub>2</sub>O, solid, ≥99.0%), sulfuric acid (H<sub>2</sub>SO<sub>4</sub>, liquid, ≥96%), and potassium hydroxide (KOH, solid, 97%) were purchased from Sinopharm Chemical Reagent Co. Ltd (Shanghai, China). Nafion<sup>®</sup> solution (5 wt%) was purchased from Alfa Aesar.

### Synthesis of Ir-Co<sub>3</sub>O<sub>4</sub> electrocatalyst

Ir-Co<sub>3</sub>O<sub>4</sub> was synthesized by the salt template method. 200 mg KCl, 0.5 mmol CoCl<sub>2</sub>·H<sub>2</sub>O, and 0.0375 mmol IrCl<sub>3</sub> (the molar ratio of CoCl<sub>2</sub>·6H<sub>2</sub>O to IrCl<sub>3</sub> is 40:3) were dissolved in 30 mL of deionized water and stirred at 90 °C for 4 h to obtain a 10 mL solution. To the above solution, 40 mg NaOH dissolved in 10 mL of deionized water was added and the mixture was stirred at 90 °C for 3 h. The dried powder was scraped to grind, spread evenly over a crucible, and heated to 350 °C in the air at a heating rate of 5 °C min<sup>-1</sup> and kept at 350 °C for 6 h. After cooling naturally, the powder was washed and filtered by pumping and dried at 60 °C for 3 h to finally obtain the Ir-Co<sub>3</sub>O<sub>4</sub> catalyst.

### Synthesis of Ru-Co<sub>3</sub>O<sub>4</sub> and Pd-Co<sub>3</sub>O<sub>4</sub> electrocatalysts

Using the above synthesis method, Ru-Co<sub>3</sub>O<sub>4</sub> and Pd-Co<sub>3</sub>O<sub>4</sub> were synthesized using RuCl<sub>3</sub> (0.0375 mmol) and PdCl<sub>2</sub> (0.0375 mmol) as sources, respectively, maintaining all other conditions.

### Synthesis of Ir-NiO, Ir-Fe<sub>2</sub>O<sub>3</sub> electrocatalysts

Using the above synthesis method, the 3d-transition metal Co source CoCl<sub>2</sub>·6H<sub>2</sub>O was replaced with Ni source NiCl<sub>2</sub>·6H<sub>2</sub>O





(0.5 mmol) and Fe source  $\text{FeCl}_3 \cdot 6\text{H}_2\text{O}$  (0.5 mmol) to synthesize Ir–NiO and Ir– $\text{Fe}_2\text{O}_3$  catalysts, respectively, and the rest of the conditions were kept unchanged.

### Synthesis of $\text{Co}_3\text{O}_4$ , NiO, and $\text{Fe}_2\text{O}_3$ electrocatalysts

$\text{Co}_3\text{O}_4$ , NiO, and  $\text{Fe}_2\text{O}_3$  catalysts were synthesized using the above synthesis method without using the noble metal precursors, and the rest of the conditions were kept unchanged.

### Characterization

Scanning electron microscopy (SEM) images were acquired using a Zeiss Supra 55 at an acceleration voltage of 5 kV. Transmission electron microscopy (TEM) and High-resolution TEM (HR-TEM) images were obtained using a JEOL 2100F instrument, operating at a voltage of 200 kV. Aberration-corrected high-angle annular dark field-scanning TEM (AC HAADF-STEM) images, along with corresponding elemental mapping, were captured on an aberration-correction Hitachi 2700D microscope operated at 200 kV. The mass fraction of Ir in Ir– $\text{Co}_3\text{O}_4$  and the dissolved ion concentrations after stability tests were analyzed using ICP-OES on an Agilent ICP-OES 730.

To further investigate the electronic structure, XPS measurements were conducted on a Thermo Scientific Escalab 250Xi with an Al– $\text{K}\alpha$  source. The XPS spectra were deconvoluted by Advantage software, and the binding energy was calibrated by C 1s (284.8 eV). The baseline was added by selecting Smart type background, and Gauss–Lorentz fitting was used for peak fitting. The position of the peak to be added was selected by moving the three vertical lines on the spectrum screen where the peaks were to be split (single peak and double peaks were selected for different binding energies according to the references). XAS of Ir  $\text{L}_{3\text{-edge}}$ , Ru K-edge, Pd K-edge, Co K-edge, Ni K-edge, and Fe K-edge were performed at the 44A beamline at the National Synchrotron Radiation Research Center (NSRRC) in Taiwan. All XAS experiments were conducted in ambient air at room temperature and analyzed using the standard program Demeter. For wavelet-transformed  $k^3$ -weighted EXAFS, the  $\chi(k)$  exported from Athena was processed using the Hama Fortran code designed by Harald Funke and Marina Chukalina. Parameters included a range of  $R$  (0–6 Å),  $k$  (0–15 Å<sup>−1</sup>),  $k$  weight (0), and the Morlet function with  $\text{kappaMorlet} = 10$ ,  $\text{sigmaMorlet} = 1$  as the mother wavelet for an encompassing distribution.

Structural analysis through XRD employed a Bruker D8 Advance powder diffractometer (operating at 40 kV, 40 mA) equipped with a Cu– $\text{K}\alpha$  source ( $\lambda = 1.5405$  Å) and fitted with a beryllium window at room temperature. Rietveld refinements for XRD data were executed with the Full-Prof program. The refined parameters comprise background parameters, line shift errors (zero shift), Caglioti coefficients ( $U$ ,  $V$ , and  $W$ ), scale factor, lattice parameters, atomic position, atomic rate occupancy, and isotropic atomic displacement parameters.

### Electrochemical measurements

The electrochemical testing of the oxygen evolution reaction performance was conducted using an electrochemical workstation (Biologic) equipped with a rotating disk electrode (RDE) device.

The workstation has a standard three-electrode cell, consisting of a carbon rod (CR) as the counter electrode, a glassy carbon electrode coated with a certain amount of catalyst as the working electrode, and a calomel electrode as the reference electrode. The tests were performed in electrolytes of 0.5 M  $\text{H}_2\text{SO}_4$  solution, 1.0 M KOH solution, and 1 × PBS solution. The final potential was calibrated to the reversible hydrogen electrode (RHE) using the equation  $E(\text{RHE}) = E(\text{Hg}|\text{HgCl}_2) + 0.0591 \times \text{pH} + 0.241$ .

The working electrode was prepared as follows: due to the poor conductivity of 3d-transition metal oxides, catalyst powder was mixed with Vulcan carbon (XC-72R, under  $\text{N}_2$  atmosphere, 400 °C, 5 °C min<sup>−1</sup>) in a 1:1 mass ratio. A homogeneous suspension was formed by dispersing 5 mg of catalyst powder and 5 mg of C powder in 1900 µL of isopropanol and sonicated for 30 min. 100 µL of 5.0 wt% Nafion<sup>®</sup> solution was added to the above suspension, and the catalyst ink was obtained by sonication of the mixed solution for 5 min. A glassy carbon electrode (with an area of 0.19625 cm<sup>2</sup>) was coated with a thin-film electrode by depositing 20 µL of the catalyst ink, followed by drying under a heat lamp.

To reach a steady state, CV measurements were performed for 10 cycles at a scan rate of 100 mV s<sup>−1</sup>. The LSV curves were later recorded at a scan rate of 5 mV s<sup>−1</sup>. The mass of all catalysts in the performance tests was 0.05 mg (254.8 µg cm<sup>−2</sup>). During the stability test, the catalyst was slowly dropped onto carbon paper, which was used as the substrate, and the catalyst ink was prepared in the same way as described above.

## Data availability

All relevant data are available from the corresponding authors upon reasonable request.

## Author contributions

J. Wang and Y. Zhu contributed equally to this work.

## Conflicts of interest

There are no conflicts to declare.

## Acknowledgements

The work leading to these results has received funding from the National Natural Science Foundation of China (22179098). We acknowledge support from the Max Planck-POSTECH-Hsinchu Center for Complex Phase Materials. N. Alonso-Vante acknowledges financial support from the European Union (ERDF) and Région Nouvelle Aquitaine.

## References

- 1 C. Hu, L. Zhang and J. Gong, *Energy Environ. Sci.*, 2019, **12**, 2620.



- 2 T. Zhang, Y.-P. Liu, Q.-T. Ye and H.-J. Fan, *J. Electrochem.*, 2022, **28**, 2214006.
- 3 W.-F. Xie and M.-F. Shao, *J. Electrochem.*, 2022, **28**, 22014008.
- 4 Y. Zhang, C. Wu, H. Jiang, Y. Lin, H. Liu, Q. He, S. Chen, T. Duan and L. Song, *Adv. Mater.*, 2018, **30**, 1707522.
- 5 H. Yang, X. Han, A. I. Douka, L. Huang, L. Gong, C. Xia, H. S. Park and B. Y. Xia, *Adv. Funct. Mater.*, 2021, **31**, 2007602.
- 6 J. Song, C. Wei, Z.-F. Huang, C. Liu, L. Zeng, X. Wang and Z. J. Xu, *Chem. Soc. Rev.*, 2020, **49**, 2196.
- 7 Y. Liu, D. Zhou, T. Deng, G. He, A. Chen, X. Sun, Y. Yang and P. Miao, *ChemSusChem*, 2021, **14**, 5359.
- 8 F.-Y. Chen, Z.-Y. Wu, Z. Adler and H. Wang, *Joule*, 2021, **5**, 1704.
- 9 I. Roger, M. A. Shipman and M. D. Symes, *Nat. Rev. Chem.*, 2017, **1**, 0003.
- 10 L. Li, P. Wang, Q. Shao and X. Huang, *Adv. Mater.*, 2021, **33**, 2004243.
- 11 D. Tang, Y. Ma, Y. Liu, K. Wang, Z. Liu, W. Li and J. Li, *J. Alloys Compd.*, 2022, **893**, 162287.
- 12 H.-F. Wang and Q. Xu, *Matter*, 2019, **1**, 565.
- 13 N.-T. Suen, S.-F. Hung, Q. Quan, N. Zhang, Y.-J. Xu and H. M. Chen, *Chem. Soc. Rev.*, 2017, **46**, 337.
- 14 K. Zhang and R. Zou, *Small*, 2021, **17**(37), 2100129.
- 15 L. Han, S. Dong and E. Wang, *Adv. Mater.*, 2016, **28**, 9266.
- 16 N. T. Suen, S. F. Hung, Q. Quan, N. Zhang, Y. J. Xu and H. M. Chen, *Chem. Soc. Rev.*, 2017, **46**, 337.
- 17 X. Zhang, C. Feng, B. Dong, C. Liu and Y. Chai, *Adv. Mater.*, 2023, **35**, 2207066.
- 18 R.-Y. Fan, Y.-N. Zhou, M.-X. Li, J.-Y. Xie, W.-L. Yu, J.-Q. Chi, L. Wang, J.-F. Yu, Y.-M. Chai and B. Dong, *Chem. Eng. J.*, 2021, **426**, 131943.
- 19 J.-Y. Xie, Z.-Z. Liu, J. Li, L. Feng, M. Yang, Y. Ma, D.-P. Liu, L. Wang, Y.-M. Chai and B. Dong, *J. Energy Chem.*, 2020, **48**, 328.
- 20 N. Yu, Y. Ma, J.-K. Ren, Z.-J. Zhang, H.-J. Liu, J. Nan, Y.-C. Li, Y.-M. Chai and B. Dong, *Chem. Eng. J.*, 2023, **478**, 147415.
- 21 H.-J. Liu, S. Zhang, W.-Y. Yang, N. Yu, C.-Y. Liu, Y.-M. Chai and B. Dong, *Adv. Funct. Mater.*, 2023, **33**, 2303776.
- 22 Z. Chen, X. Duan, W. Wei, S. Wang and B.-J. Ni, *Nano Energy*, 2020, **78**, 105270.
- 23 L. Hou, H. Jang, H. Liu, Z. Li, M. G. Kim, Q. Qin and X. Liu, *ACS Sustainable Chem. Eng.*, 2022, **10**, 15950.
- 24 L. Zhang, Y. Wang, Y. Wang, H. Liu, Q. Qin and X. Liu, *ACS Sustainable Chem. Eng.*, 2022, **10**, 10658.
- 25 G. Wu, A. Santandreu, W. Kellogg, S. Gupta, O. Ogoke, H. Zhang, H.-L. Wang and L. Dai, *Nano Energy*, 2016, **29**, 83.
- 26 T. R. Cook, D. K. Dogutan, S. Y. Reece, Y. Surendranath, T. S. Teets and D. G. Nocera, *Chem. Rev.*, 2010, **110**, 6474.
- 27 G. Wu, X. Zheng, P. Cui, H. Jiang, X. Wang, Y. Qu, W. Chen, Y. Lin, H. Li, X. Han, Y. Hu, P. Liu, Q. Zhang, J. Ge, Y. Yao, R. Sun, Y. Wu, L. Gu, X. Hong and Y. Li, *Nat. Commun.*, 2019, **10**, 4855.
- 28 Y. Xie, Y. Su, H. Qin, Z. Cao, H. Wei, F. Wu and G. Ou, *Int. J. Hydrogen Energy*, 2023, **48**, 14642.
- 29 S. Kalantarifard, S. I. Allakhverdiev and M. M. Najafpour, *Int. J. Hydrogen Energy*, 2020, **45**, 33563.
- 30 S. Mehrabani, R. Bikas, Z. Zand, Y. Mousazade, S. I. Allakhverdiev and M. M. Najafpour, *Int. J. Hydrogen Energy*, 2020, **45**, 17434.
- 31 Z. Lei, W. Cai, Y. Rao, K. Wang, Y. Jiang, Y. Liu, X. Jin, J. Li, Z. Lv, S. Jiao, W. Zhang, P. Yan, S. Zhang and R. Cao, *Nat. Commun.*, 2022, **13**, 24.
- 32 T. G. Yun, Y. Heo, H.-B. Bae and S.-Y. Chung, *Nat. Commun.*, 2021, **12**, 824.
- 33 A. L. Bhatti, A. Tahira, A. Gradone, R. Mazzaro, V. Morandi, U. Aftab, M.-I. Abro, A. Nafady, K. Qi, A. Infantes-Molina, A. Vomiero and Z. H. Ibupoto, *Electrochim. Acta*, 2021, **398**, 139338.
- 34 Q. Wang, Z. Zhang, C. Cai, M. Wang, Z. L. Zhao, M. Li, X. Huang, S. Han, H. Zhou, Z. Feng, L. Li, J. Li, H. Xu, J. S. Francisco and M. Gu, *J. Am. Chem. Soc.*, 2021, **143**, 13605.
- 35 Y. Tong, P. Chen, L. Chen and X. Cui, *ChemSusChem*, 2021, **14**, 2576.
- 36 P. Zhang, L. Li, D. Nordlund, H. Chen, L. Fan, B. Zhang, X. Sheng, Q. Daniel and L. Sun, *Nat. Commun.*, 2018, **9**, 381.
- 37 J. Yu, Q. He, G. Yang, W. Zhou, Z. Shao and M. Ni, *ACS Catal.*, 2019, **9**, 9973.
- 38 Y. Dai, J. Yu, J. Wang, Z. Shao, D. Guan, Y.-C. Huang and M. Ni, *Adv. Funct. Mater.*, 2022, **32**, 2111989.
- 39 M. Xiao, J. Zhu, S. Li, G. Li, W. Liu, Y.-P. Deng, Z. Bai, L. Ma, M. Feng, T. Wu, D. Su, J. Lu, A. Yu and Z. Chen, *ACS Catal.*, 2021, **11**, 8837.
- 40 Z. Shi, Y. Wang, J. Li, X. Wang, Y. Wang, Y. Li, W. Xu, Z. Jiang, C. Liu, W. Xing and J. Ge, *Joule*, 2021, **5**, 2164.
- 41 J. Yin, J. Jin, M. Lu, B. Huang, H. Zhang, Y. Peng, P. Xi and C.-H. Yan, *J. Am. Chem. Soc.*, 2020, **142**, 18378.
- 42 X. Liang, L. Shi, R. Cao, G. Wan, W. Yan, H. Chen, Y. Liu and X. Zou, *Adv. Mater.*, 2020, **32**, 2001430.
- 43 E. Oakton, D. Lebedev, M. Povia, D. F. Abbott, E. Fabbri, A. Fedorov, M. Nachtegaal, C. Copéret and T. J. Schmidt, *ACS Catal.*, 2017, **7**, 2346.
- 44 W. Hu, S. Chen and Q. Xia, *Int. J. Hydrogen Energy*, 2014, **39**, 6967.
- 45 H.-S. Oh, H. N. Nong, T. Reier, A. Bergmann, M. Gliech, J. Ferreira de Araújo, E. Willinger, R. Schlögl, D. Teschner and P. Strasser, *J. Am. Chem. Soc.*, 2016, **138**, 12552.
- 46 Q. Wang, X. Huang, Z. L. Zhao, M. Wang, B. Xiang, J. Li, Z. Feng, H. Xu and M. Gu, *J. Am. Chem. Soc.*, 2020, **142**, 7425.
- 47 Y. Zhu, J. Wang and J. Ma, *Small Sci.*, 2023, **3**, 2300010.
- 48 J. Yang, W. Li, D. Wang and Y. Li, *Small Struct.*, 2021, **2**, 2000051.
- 49 J. Liu, *ACS Catal.*, 2017, **7**, 34.
- 50 Q. Wang, Y. Lei, Y. Wang, Y. Liu, C. Song, J. Zeng, Y. Song, X. Duan, D. Wang and Y. Li, *Energy Environ. Sci.*, 2020, **13**, 1593.
- 51 Y. Cui, Z. Cao, Y. Zhang, H. Chen, J. Gu, Z. Du, Y. Shi, B. Li and S. Yang, *Small Sci.*, 2021, **1**, 2100017.
- 52 X. Li, H. Rong, J. Zhang, D. Wang and Y. Li, *Nano Res.*, 2020, **13**, 1842.
- 53 X.-F. Yang, A. Wang, B. Qiao, J. Li, J. Liu and T. Zhang, *Acc. Chem. Res.*, 2013, **46**, 1740.
- 54 C.-W. Tung, Y.-Y. Hsu, Y.-P. Shen, Y. Zheng, T.-S. Chan, H.-S. Sheu, Y.-C. Cheng and H. M. Chen, *Nat. Commun.*, 2015, **6**, 8106.
- 55 K. Fominykh, G. C. Tok, P. Zeller, H. Hajiyani, T. Miller, M. Döblinger, R. Pentcheva, T. Bein and D. Fattakhova-Rohlfing, *Adv. Funct. Mater.*, 2017, **27**, 1605121.



- 56 W. Wang, S. Xi, Y. Shao, X. Gao, J. Lin, C. Meng, W. Wang, X. Guo and G. Li, *ChemElectroChem*, 2019, **6**, 1846.
- 57 Y. Wang, X. Cui, J. Zhang, J. Qiao, H. Huang, J. Shi and G. Wang, *Prog. Mater. Sci.*, 2022, **128**, 100964.
- 58 L. Wang, M.-X. Chen, Q.-Q. Yan, S.-L. Xu, S.-Q. Chu, P. Chen, Y. Lin and H.-W. Liang, *Sci. Adv.*, 2019, **5**, eaax6322.
- 59 S. Zhao, R. Jin and R. Jin, *ACS Energy Lett.*, 2018, **3**, 452.
- 60 D. Hu, R. Wang, P. Du, G. Li, Y. Wang, D. Fan and X. Pan, *Ceramics Int.*, 2022, **48**, 6549.
- 61 Y. Huan, J. Shi, X. Zou, Y. Gong, C. Xie, Z. Yang, Z. Zhang, Y. Gao, Y. Shi, M. Li, P. Yang, S. Jiang, M. Hong, L. Gu, Q. Zhang, X. Yan and Y. Zhang, *J. Am. Chem. Soc.*, 2019, **141**, 18694.
- 62 X. Xiao, H. Song, S. Lin, Y. Zhou, X. Zhan, Z. Hu, Q. Zhang, J. Sun, B. Yang, T. Li, L. Jiao, J. Zhou, J. Tang and Y. Gogotsi, *Nat. Commun.*, 2016, **7**, 11296.
- 63 T.-Y. Jeon, S.-H. Yu, S.-J. Yoo, H.-Y. Park and S.-K. Kim, *Carbon Energy*, 2021, **3**, 8.
- 64 D. Guan, G. Ryu, Z. Hu, J. Zhou, C.-L. Dong, Y.-C. Huang, K. Zhang, Y. Zhong, A. C. Komarek, M. Zhu, X. Wu, C.-W. Pao, C.-K. Chang, H.-J. Lin, C.-T. Chen, W. Zhou and Z. Shao, *Nat. Commun.*, 2020, **11**, 3376.
- 65 Y. Zhu, J. Wang, T. Koketsu, M. Kroschel, J.-M. Chen, S.-Y. Hsu, G. Henkelman, Z. Hu, P. Strasser and J. Ma, *Nat. Commun.*, 2022, **13**, 7754.
- 66 V. Pfeifer, T.-E. Jones, J.-J. Velasco Vélez, R. Arrigo, S. Piccinin, M. Hävecker, A. Knop-Gericke and R. Schlögl, *Chem. Sci.*, 2017, **8**, 2143.
- 67 B. Guo, R. Ma, Z. Li, J. Luo, M. Yang and J. Wang, *Mater. Chem. Front.*, 2020, **4**, 1390.
- 68 F. Jiao and H. Frei, *Angew. Chem., Int. Ed.*, 2009, **48**, 1841.

